

pubs.acs.org/JPCC Article

Elucidating the Degradation Mechanisms in Silicon Telluride through Multimodal Characterization

Evan Hathaway, Roberto Gonzalez Rodriguez, Yuankun Lin, and Jingbiao Cui*



Cite This: J. Phys. Chem. C 2023, 127, 13800–13809



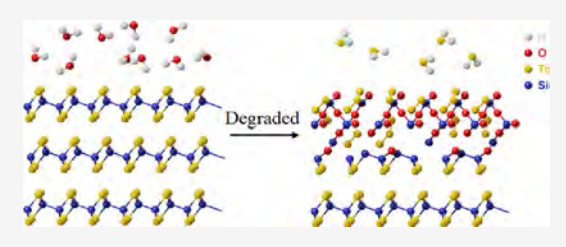
ACCESS I

III Metrics & More

Article Recommendations

s Supporting Information

ABSTRACT: Silicon telluride (Si_2Te_3) and many other tellurium-containing compounds show emergent Raman peaks located at ~120 and ~140 cm⁻¹ as they age. The origin of these two emergent peaks is controversial in the literature and has been attributed to myriad causes such as the intrinsic Raman modes of the telluride materials, surface oxidation, defects, double resonances, and tellurium precipitates. The controversial nature of these peaks has led to the misidentification of highly degraded materials as pristine and to the misinterpretation of changes in Raman spectra. Here, we present a



comprehensive and multimodal study on $\mathrm{Si_2Te_3}$ thin films and bulk crystals grown by a chemical vapor deposition process. We find that the two emergent Raman peaks originate from tellurium nanocrystallites formed in the degraded surface layers of $\mathrm{Si_2Te_3}$. The formation of the tellurium nanocrystallites is shown to be a result of a hydrolysis process in which $\mathrm{Si_2Te_3}$ reacts with atmospheric water vapor. This study unambiguously clarifies the origin of the controversial Raman peaks seen in numerous telluride compounds and provides a blueprint for the accurate characterization of these material systems in the future.

1. INTRODUCTION

Since the discovery of graphene in 2004, the field of nano/two-dimensional materials has exploded in popularity. Of interest in this growing field is the diverse family of material compounds containing tellurium. These materials vary drastically in function, crystalline structure, morphology, and electronic and optical properties. Raman spectroscopy is a common method used in the characterization of these telluride compounds, and, despite their diversity, two emergent Raman peaks located between ~120 and ~140 cm⁻¹ can be generally observed in these materials.

These modes are emergent in that they most often are not found in pristine samples and arise as the samples age, sometimes completely preventing the observation of the original intrinsic Raman modes of the sample. The peaks are broad with the lower wavenumber peak always being of higher intensity than that of the higher wavenumber peak. The lower wavenumber peak is usually located between 119 and 130 cm⁻¹, while the higher wavenumber peak is located between 139 and 145 cm⁻¹. These two Raman modes have caused a great deal of controversy in the study of the materials in which they arise, and their cause has been attributed to intrinsic Raman modes of the sample, general surface oxidation, defects, dopant concentrations, double resonances, and tellurium precipitates, to name a few.

Materials in which these two emergent Raman modes have been observed include binary compounds of tellurium such as Si₂Te₃, ² ZnTe, ³ CdTe, ^{4,5} GaTe, ^{1,6,7} ZrTe₃, ⁶ SnTe, ⁸ PbTe, ⁸ GeTe, ⁹ Bi₂Te₃, ¹ As₂Te₃, ¹ and Sb₂Te₃, ¹⁰ ternary compounds such as PbSnTe, ^{5,11} HgCdTe, ⁵ GaGeTe, ¹ SnBi₂Te₄, ¹ and SnSb₂Te₄; ¹² and quaternary compounds such as

Cu₂ZnSnTe₄^{13,14} and CdS_{1-x-y}Se_xTe_y¹⁴ among others. We have previously studied these emergent Raman peaks in Si₂Te₃² and found them most likely to be the result of a hydrolysis process, first described by Bailey,¹⁵ in which Si₂Te₃ reacts with moisture in the air forming amorphous SiO₂ and H₂Te, the latter of which spontaneously decomposes into H₂ and Te. This explanation is in agreement with the findings of Manjón et al.,¹ who studied these emergent peaks in several other tellurium-containing compounds and found them to be caused by the precipitation of tellurium of nanometric size. However, this explanation remains incomplete since it relies almost entirely upon Raman spectroscopy to draw conclusions.

Si₂Te₃ is a p-type semiconductor with a unique layered trigonal structure, with silicon dimers occupying two-thirds of the octahedral vacancies created between HCP Te atoms. The dimers may take on one of four possible orientations offering the ability to tune the optical and electrical properties through the manipulation of dimer orientation. Its chemical tunability, optical anisotropic properties, and photosensitivity make it an ideal candidate for optoelectronic devices. Si₂Te₃ nanotubes have also been shown to display resistive switching behaviors useful in resistive memory devices. Despite these numerous demonstrated benefits,

Received: March 20, 2023 Revised: June 2, 2023 Published: July 5, 2023





little effort has been made to ensure that Si₂Te₃-based devices remain pristine after the fabrication and testing of such devices.

Here, we expand upon our previous work by studying the degradation of $\mathrm{Si_2Te_3}$ thin films and bulk crystals using X-ray photoelectron spectroscopy (XPS), X-ray powder diffraction (XRD), atomic force microscopy (AFM), and ultraviolet—visible—near infrared (UV—vis—NIR) spectroscopy in conjunction with Raman spectroscopy. For the first time, a modified chemical vapor deposition (CVD) method is used to grow high-quality $\mathrm{Si_2Te_3}$ thin films and bulk crystals. We offer evidence that the degraded $\mathrm{Si_2Te_3}$ consists of a thin surface layer of amorphous $\mathrm{SiO_2}$ with embedded nanocrystals of $\mathrm{TeO_2}$ followed by a layer of amorphous $\mathrm{SiO_2}$ with embedded nanocrystallites of tellurium.

2. EXPERIMENTAL METHODS

2.1. Bulk Crystal and Thin Film Sample Preparation. Figure 1 shows a schematic of the modified CVD apparatus

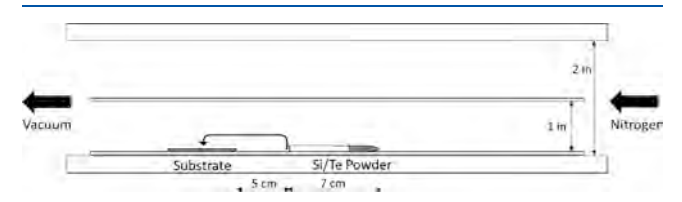


Figure 1. Modified CVD setup for the deposition of $\mathrm{Si_2Te_3}$ thin films and bulk crystals.

used to grow both the bulk crystals and thin films of ${\rm Si_2Te_3}$. A 1 in.-diameter quartz tube was nested inside an outer 2 in.-diameter quartz tube and placed inside an Across International STF 1200 600 mm-length tube furnace. The 1 in. quartz tube confines the evaporated source materials to a smaller volume, which reduces the amount of source material needed for sample growth. A 7 cm-long quartz tube with one end sealed was then filled with stoichiometric amounts of silicon (325 mesh, 99%) and tellurium (30 mesh, 99.997%) powders acquired from Sigma-Aldrich and placed in the center of the tube furnace. The 7 cm tube slows the release of source material and helps to direct most of the evaporated powders toward the downstream substrate.

A glass or silicon substrate was put 5 cm from the edge of the open end of the 7 cm quartz tube. The entire apparatus was then evacuated, and a constant flow of 80 sccm nitrogen was flowed through the tube maintaining a pressure of $\sim\!5000$ mTorr. The tube was then heated from room temperature to 300 °C at a slow rate of 10 °C/min. After reaching 300 °C, the temperature was increased to 850 °C at the maximum heating rate of 30 °C/min. Once 850 °C was reached, the temperature was held stable for 5 min before allowing to cool back to room temperature.

To grow a bulk crystal vs thin film, one only needs to change the amount of source material added into the 7 cm quartz tube along with the length of the cooling time. In order to grow thin films, ~80 mg of tellurium powder and ~60 mg of silicon powder were mixed in the 7 cm tube. Immediately after growth, the sample was rapidly cooled back to room temperature by opening the tube furnace. For the bulk crystal, 300 mg of tellurium and 200 mg of silicon powder were loaded and mixed in the 7 cm tube. After growth, the sample was allowed to slowly cool back to room temperature without opening the tube furnace. The total growth time, including

cooling, was about 1.5 and 4.5 h for the thin film and bulk crystal samples, respectively.

2.2. Material Characterization. All Raman spectra were taken using a Renishaw InVia Raman microscope with a laser excitation wavelength of 532 nm. Because $\mathrm{Si}_2\mathrm{Te}_3$ has been previously shown to be sensitive to laser intensity, all measurements were taken at a low laser power of 25 $\mu\mathrm{W}$ with a 3 s exposure time. For maximum spatial and spectral resolution, a 100× objective and 1800 lines/mm grating were used

The morphologies of the thin film and exfoliated bulk crystal samples were characterized using an FEI Quanta 200 environmental scanning electron microscope (SEM) along with a Veeco Multimode Nanoscope III scanning probe microscope for AFM. SEM images of the thin film were taken at points corresponding to different film thicknesses, while AFM measurements were taken at a central point of the film.

XPS depth profiling was carried out using a PHI 5000 VersaProbe scanning XPS microprobe. Thin film and bulk crystal samples grown on silicon substrates were loaded into an evacuated sample chamber. Samples were located and aligned using built-in SXI imaging. Each XPS spectrum included in the depth profiles was taken after 1 min cycles of Ar sputtering at an accelerating voltage of 3 keV with charge compensation active. The sputtering depth was calibrated by taking AFM cross-sectional profiles before and after 10 sputtering cycles as shown in Figure S1 of the Supporting Information.

Micro UV-vis-NIR spectroscopy of thin films and exfoliated flakes was performed using a modified optical microscope, ²² with an enhanced near-IR illumination source. XRD measurements of thin films were taken with the use of a Rigaku Miniflex 600.

3. RESULTS AND DISCUSSION

In this study, we use both thin film and bulk crystalline morphologies to further study the degradation of $\mathrm{Si_2Te_3}$. Both of the techniques used to grow these morphologies are being published here for the first time. Thin films of $\mathrm{Si_2Te_3}$ have previously been grown and characterized in the literature, but the quality and composition of these films are questionable as they show strong Raman modes at ~120 and 140 cm⁻¹, suggesting that they are either highly degraded or consist entirely of tellurium.²³ Bulk crystals have also previously been grown; however, they use CVT techniques that require sealed evacuated ampules and take weeks to grow. Also, the composition of these bulk crystals is again in question because the included XPS data show strong Si 2p peak binding energies at ~103 eV suggesting the presence of $\mathrm{SiO_2}$, and the measured photoluminescence does not match that of previously published results involving $\mathrm{Si_2Te_3}$.

A modified CVD technique is used to grow both the thin films and bulk crystals used in this study. A detailed explanation of this process can be found in the Experimental Methods section. Images of typical samples for both morphologies can be found in Figure S2 of the Supporting Information. Bulk crystals range in size from ~0.5 to 3 mm. The thin film thickness varies along the downstream axis of the substrate with the thickness decreasing as the distance from the source material increases. SEM and AFM images of freshly grown thin films can be found in Figures S3 and S4 in the Supporting Information. From these images, it is clear that the films are polycrystalline in nature given the numerous particles present. Also of note is that, as shown in Figure S3, the particle

size changes with the downstream axis with larger crystallites located closer to the source material.

Figure 2 shows the typical Raman spectrum of freshly grown Si₂Te₃, marked by a single intrinsic Raman peak located at 145

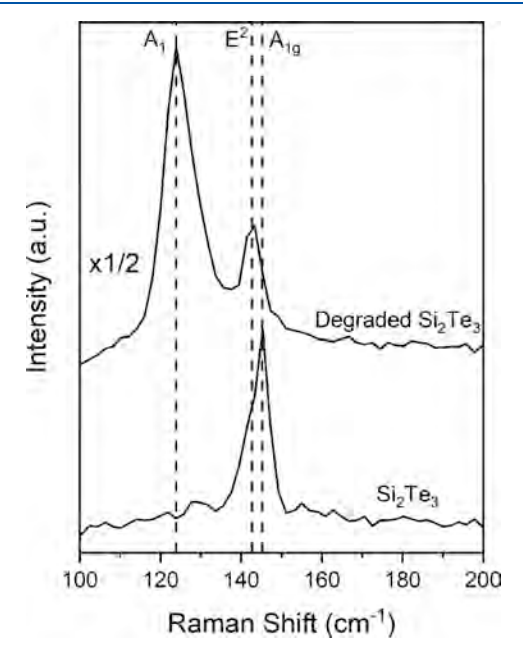


Figure 2. Typical Raman spectra of freshly grown and aged samples of $\mathrm{Si}_2\mathrm{Te}_3$.

cm $^{-1}$, which has been assigned as the A_{1g} mode in the literature. Also shown in Figure 2 is the typical Raman spectrum of an aged sample of Si_2Te_3 , which shows the controversial emergent Raman peaks at 124 and 142 cm $^{-1}$. In our previous work, we have shown these emergent Raman peaks to most likely be a result of tellurium accumulation at the degraded surface layers and have identified them as the A_1 and E^2 modes of tellurium, respectively. We should also note the presence of a small shoulder located at 142 cm $^{-1}$ for the freshly grown sample, which is attributed to the E^2 mode of tellurium. This suggests that in the short time (~ 30 min) between the growth of the material and the collection of the Raman spectrum, the sample has already begun to show signs of degradation.

The Raman peak intensity of the degraded Si₂Te₃ is larger than that of the pristine sample and has been reduced by half in Figure 2 to improve readability. Tellurium is known to have a large scattering cross section with visible light, which would both explain the enhanced intensity of the Raman modes at \sim 120 and \sim 140 cm⁻¹ and the reduction in the intrinsic Si₂Te₃ Raman mode at ~144 cm⁻¹ due to the greatly reduced penetration depth of the laser. 4,29 In fact, the penetration depth of a 532 nm laser in tellurium can be calculated from the known complex index of refraction³⁰ to be ~14.7 nm. This small penetration depth means that even an extremely thin layer of tellurium can greatly influence the Raman spectrum. The amount of time that it takes for tellurium-containing materials to degrade is highly variable with some, such as Si₂Te₃, taking a few hours to days for the emergent tellurium Raman peaks to dominate, while others, such as PbTe, can take years.8

The linewidths of the emergent peaks are greater than one might expect for Raman-active modes. The broad width of these peaks can be explained, in part, by the nanometric nature of the tellurium precipitates. The different sized tellurium nanocrystallites will each give rise to Raman-active modes of differing wavenumber. The observed emergent Raman peaks are a convolution of these resulting Raman modes resulting in their broad linewidths. Also, as pointed out by Manjón et al., strain in the segregated tellurium precipitates at the surface of the sample may also explain this broad linewidth, although the effect is minor compared to the nanometric size of the tellurium precipitates. The convolution of these many Raman-active modes may also explain the inconsistent peak positions of the emergent A_1 and E^2 modes seen in the literature, although we should also point out that different Raman system configurations (laser intensity, grating density, etc.) will also greatly affect the peak positions.

To better understand the precise compositional changes of the degraded Si₂Te₃, an XPS depth profile was performed for both the thin film and bulk crystal samples. Figure 3a shows

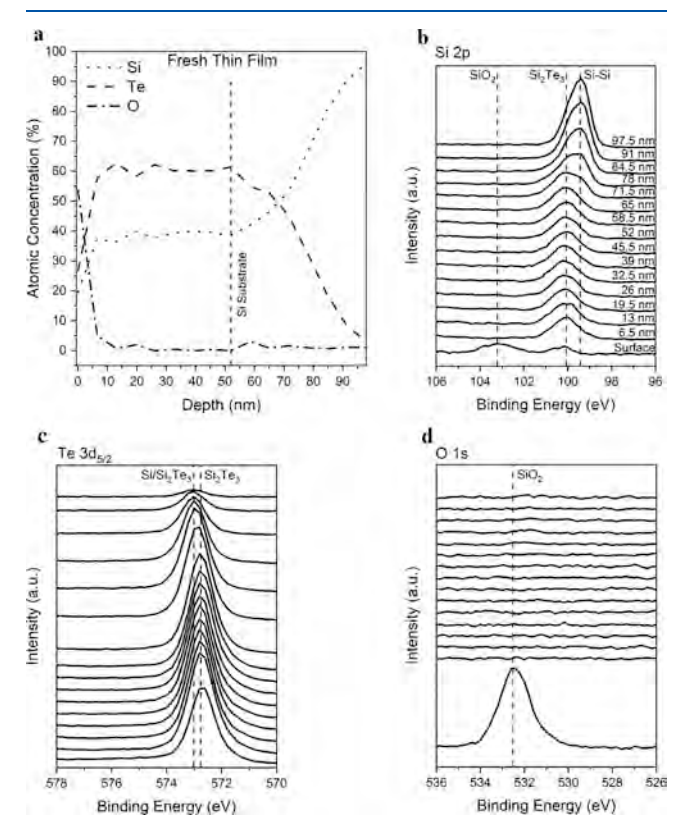


Figure 3. XPS (a) depth profile and analysis of (b) Si, (c) Te, and (d) O for the freshly grown Si₂Te₃ thin film on a Si substrate.

the XPS depth profile for a freshly grown thin film of Si₂Te₃. The background for all XPS peaks was fit using Shirley backgrounds in PHI Multipak and subtracted before determining the compositional contributions of each peak. The surface of the freshly grown sample has a large amount of oxygen due to the sample's exposure to air, which is consistent with the beginning of the hydrolysis process oxidizing the surface layers of Si resulting in SiO₂. After a single sputtering step, this oxygen-rich area is completely removed revealing the underlying pristine material with the expected 2:3, silicon to tellurium, stoichiometry of Si₂Te₃. After reaching a depth of 52 nm, the proportion of silicon begins to drastically increase. This drastic increase is due to portions of the film being

completely etched away, revealing the underlying silicon substrate. The vertical line labeled "Si Substrate" in Figure 3a marks the point after which the silicon signal from the substrate can be seen emerging.

Only by performing a detailed analysis of the XPS depth profile spectra can conclusions be drawn about the nature of the chemical bonds in the sample. Figure 3b-d shows the XPS profile analysis of silicon, tellurium, and oxygen. The sputtering depth for each spectrum is labeled in Figure 3b and also corresponds to the spectra found in Figure 3c,d. Tellurium has two characteristic XPS peaks belonging to the $3d_{3/2}$ and $3d_{5/2}$ orbitals. Figure S5a in the Supporting Information shows the XPS analysis of tellurium in the thin film including both of these peaks. A careful fit of the two peaks using Voigt functions was performed and is demonstrated in Figure S5b of the Supporting Information. The integrated peak area ratio was determined to be 1.47, which is close to the expected 3/2 ratio between the $3d_{5/2}$ and $3d_{3/2}$ orbitals. The $3d_{3/2}$ peak can be seen changing in intensity and position along with the $3d_{5/2}$ peak. Note that we only use the $3d_{5/2}$ peak for compositional analysis in this study.

The surface Si 2p spectrum shows two peaks located at 100.1 and 103.2 eV. The peak at 103.2 eV is consistent with Si–O binding in $\mathrm{SiO_2}^{31}$ while the peak at 100.1 eV is due to Si–Te binding in $\mathrm{Si_2Te_3}$. Further confirming the presence of $\mathrm{SiO_2}$ is the initial O 1s peak located at 532.4 eV, which is also consistent with Si–O binding in $\mathrm{SiO_2}^{31}$ The initial Te $\mathrm{3d_{5/2}}$ spectrum shows a singular peak located at 572.7 eV, which is associated with Si–Te binding in $\mathrm{Si_2Te_3}$. These initial spectra suggest that it is silicon that oxidizes leaving a thin $\mathrm{SiO_2}$ layer at the surface of even freshly grown samples.

After a single sputter step, the Si 2p and O 1s peaks located at 103.2 and 532.4 eV, respectively, disappear, while the Si 2p and Te $3d_{5/2}$ peaks at 100.1 and 572.7 eV, respectively, increase in intensity. This indicates that the degraded layer containing SiO₂ is completely removed leaving behind only the pristine Si₂Te₃ layers. The fact that it only took a sputtering depth of 6.5 nm to completely remove the degraded layers indicates that these degraded layers were very thin, as expected for freshly grown samples.

As sputtering continues into the bulk of the thin film, the spectra remain very consistent until a depth of 52 nm is reached. After 52 nm, a new Si 2p peak emerges at 99.4 eV as shown in Figure 3b. This new peak continues to increase until it eventually dominates the Si₂Te₃-associated peak located at 100.1 eV. This emerging peak is consistent with Si–Si binding in elemental silicon and can be explained by the complete removal of Si₂Te₃ due to sputtering, exposing the underlying silicon substrate. This is further confirmed by the drastic decrease in the intensity of the Si₂Te₃-associated Te 3d_{5/2} peak in Figure 3c after a depth of 52 nm is reached. Also of note is the slight shift in the peak position of the Te 3d_{5/2} peak from 572.7 to 573.0 eV after a depth of 71.5 nm. This shift is most likely due to surface interactions at the Si/Si₂Te₃ interface.

Figure 4 shows the XPS depth profile (Figure 4a) and profile analysis (Figure 4b-d) for a film grown concurrently with the one studied in Figure 3 but after being aged under ambient conditions for 24 h. The initial spectra taken before sputtering (Figure 4b-d) show peaks at 103.2 eV for Si 2p, 573.0 and 576.2 eV for Te $3d_{5/2}$, and 530.5 and 532.4 eV for O 1s. Similar to that of the freshly grown thin film, the peaks at 103.2 and 532.4 eV are consistent with Si-O binding in SiO₂. However, unlike the fresh thin film, there is no Si 2p peak at

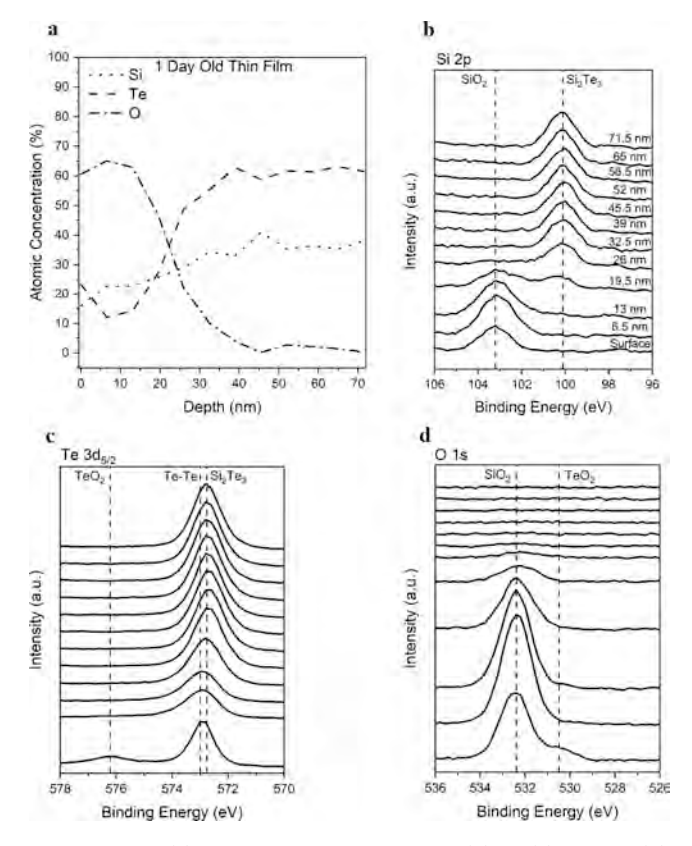


Figure 4. XPS (a) depth profile and analysis of (b) Si, (c) Te, and (d) O for the 24 h-old Si₂Te₃ thin film grown on a Si substrate.

100.1 eV, and the Te $3d_{5/2}$ peak is located at 573.0 eV rather than 572.7 eV, suggesting that there is no Si–Te binding at the surface, and instead, it is Te–Te binding consistent with the formation of elemental tellurium.³³ Another difference between the unsputtered surfaces of freshly grown and aged samples is the appearance of a Te $3d_{5/2}$ peak located at 576.2 eV along with an O 1s shoulder located at 530.5 eV, both of which are indicative of Te–O binding in TeO₂.³⁴

After a single sputtering cycle, equating to a depth of 6.5 nm, the Te $3d_{5/2}$ peak at 576.2 eV and the O 1s shoulder at 530.5 eV associated with TeO2 disappear, showing that TeO2 is present in only a thin surface layer. This very thin surface layer of TeO2 has been used by others as proof of Te-O binding in the bulk of the degraded layers; however, that is clearly not the case.^{6,7} In contrast, the Si 2p peak at 103.2 eV and the O 1s peak at 532.4 eV associated with SiO₂ disappear only after a depth of 39 nm is reached. This is clear evidence that it is SiO₂, and not TeO2, which extends into the bulk of the degraded layers and is consistent with the hydrolysis process outlined earlier. After reaching a depth of 26 nm, a Si 2p peak at 100.1 eV emerges, and the Te 3d_{5/2} peak, which was at 573.0 eV, shifts to 572.7 eV, both of which are consistent with Si-Te binding in Si₂Te₃. This shows that between the upper degraded layers and lower pristine layers, there is a transitionary inhomogeneous layer where both SiO2, Te, and Si2Te3 exist.

The depth profile shown in Figure 4a clearly shows a tellurium deficiency in the degraded layers where SiO_2 is present. This deficiency can be explained by the sublimation of tellurium from the surface as water reacts with Si_2Te_3 resulting in gaseous hydrogen telluride (H_2Te). Hydrogen telluride is a highly volatile compound, which quickly degrades into H_2 and Te at room temperature. It is likely that some of the hydrogen

telluride escapes the surface of the sample before degrading, while some remains trapped in the degraded layers. It should also be noted that freshly grown $\mathrm{Si_2Te_3}$ has a strong odor reminiscent of garlic consistent with the formation of $\mathrm{H_2Te}$, which is known to have a strong odor even at exceptionally low concentrations.

Deconvolution of the Te $3d_{5/2}$ XPS peaks shown in Figure 4c was carried out in order to better illustrate the slight shift in the peak position as the aged thin film was sputtered. The spectra were deconvoluted using Voigt functions as demonstrated in Figure 5a for the spectrum taken after reaching a

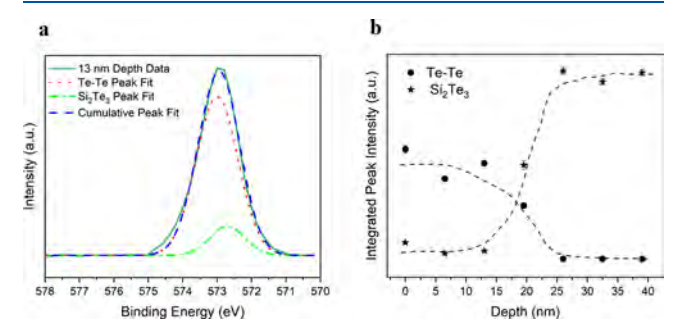


Figure 5. (a) Deconvolution of the Te $3d_{5/2}$ XPS peak at a depth of 13 nm and (b) integrated peak intensities as a function of sputtering depth.

depth of 13 nm. The data can be well fit by two peaks with centers located at 572.7 and 573.0 eV corresponding to Si–Te and Te–Te binding, respectively. Figure 5b plots the integrated intensities of the deconvoluted peaks vs sputtering time, with dashed lines drawn to help guide the eyes. Initially, the Te–Te-associated peak dominates the spectra. The Si–Te-associated peak gradually increases as the sputtering depth increases until eventually, at a depth of 26 nm, it is the only peak remaining. This only cements our earlier conclusion that it is pure tellurium that resides in the degraded layers of $\mathrm{Si}_2\mathrm{Te}_3$ followed by a transitionary inhomogeneous layer of SiO_2 , Te, and $\mathrm{Si}_2\mathrm{Te}_3$, which is then finally followed by the undegraded pristine $\mathrm{Si}_2\mathrm{Te}_3$.

Raman spectra of the Si₂Te₃ thin films studied in Figures 3 and 4 were taken immediately after growth, after being aged for 24 h, and after completing 11 Ar sputtering cycles. These spectra can be seen in Figure S6 of the Supporting Information. The Raman spectrum of the freshly grown sample shows a strong intrinsic Si₂Te₃ A_{1g} peak at ~144 cm⁻¹ along with a small peak and shoulder at ~ 120 and ~ 140 cm⁻¹, respectively, which we have previously discussed as being the A₁ and E² peaks of crystalline tellurium. After aging, the intrinsic A_{1g} peak of Si₂Te₃ has a weaker intensity, while the A₁ peak of tellurium can be seen increasing in intensity. The increase of this A₁ peak coincides with the formation of SiO₂ and tellurium as evidenced by the XPS spectra in Figure 5. After sputtering, the Raman spectrum returns to showing a single strong Raman peak at ~144 cm⁻¹, which coincides with the XPS spectra in Figure 5 showing a return to the expected stoichiometry of pristine Si₂Te₃. This solidifies the fact that the observed changes in the Raman spectra of Si₂Te₂ are due to changes in the composition of the degraded surface layers.

The same XPS profiling procedure, which was carried out on the thin film, was also carried out for a freshly grown and aged bulk Si₂Te₃ crystal. Figure 6 shows the XPS depth profile (Figure 4a) and profile analysis (Figure 4b–d) for the freshly

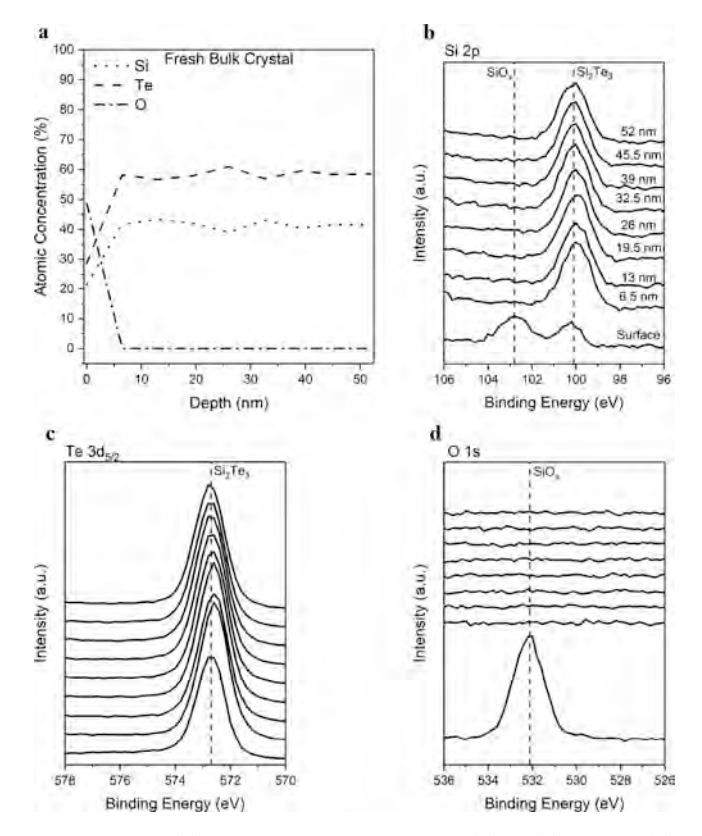


Figure 6. XPS (a) depth profile and analysis of (b) Si, (c) Te, and (d) O for freshly grown Si₂Te₃ bulk crystals on a Si substrate.

grown bulk crystal. The depth profile, similar to that of the thin film, initially shows a large concentration of oxygen and a slight tellurium deficiency. Again, this high oxygen concentration and slight tellurium deficiency can be explained by the previously discussed hydrolysis process. After a single sputtering step, oxygen has been completely removed, and the silicon to tellurium atomic concentration returns to the expected 2:3 stoichiometry of pristine $\mathrm{Si}_2\mathrm{Te}_3$.

The XPS analysis shows the expected Si₂Te₃-associated peaks at 100.1 eV for Si 2p and 572.7 eV for Te 3d_{5/2}. However, the oxygen-related peaks present in the initial spectra are slightly lower than the binding energies expected for SiO₂. As discussed for the thin films, the binding energies for SiO₂ for Si 2p and O 1s should occur at 103.2 and 532.4 eV. Figure 6b,d shows Si 2p and O 1s peaks at binding energies of 532.2 and 102.8 eV, respectively. The most likely cause for this shift away from the expected SiO₂ binding energies is the formation of silicon suboxides, SiO_x , which have been shown to result in shifts to lower binding energies.^{35,36} The existence of SiO_x rather than SiO₂ suggests that the surface layer of the bulk crystal has oxygen vacancies simply because it has not had the time necessary to fully react with moisture in air. Because the overall surface area of the bulk crystal is smaller than that of the thin film, we can expect it to degrade slower. This is why we do not see SiO_x peaks in the thin film sample.

Figure 7 shows the XPS depth profile (Figure 7a) and profile analysis (Figure 7b-d) for the same bulk crystal studied in Figure 6 but after being aged under ambient conditions for one day. Again, similar to that of the aged thin film, the bulk crystal initially has a high oxygen concentration along with a tellurium concentration lower than that of silicon. Unlike the thin film, however, it only takes the removal of 19.5 nm vs 39 nm of

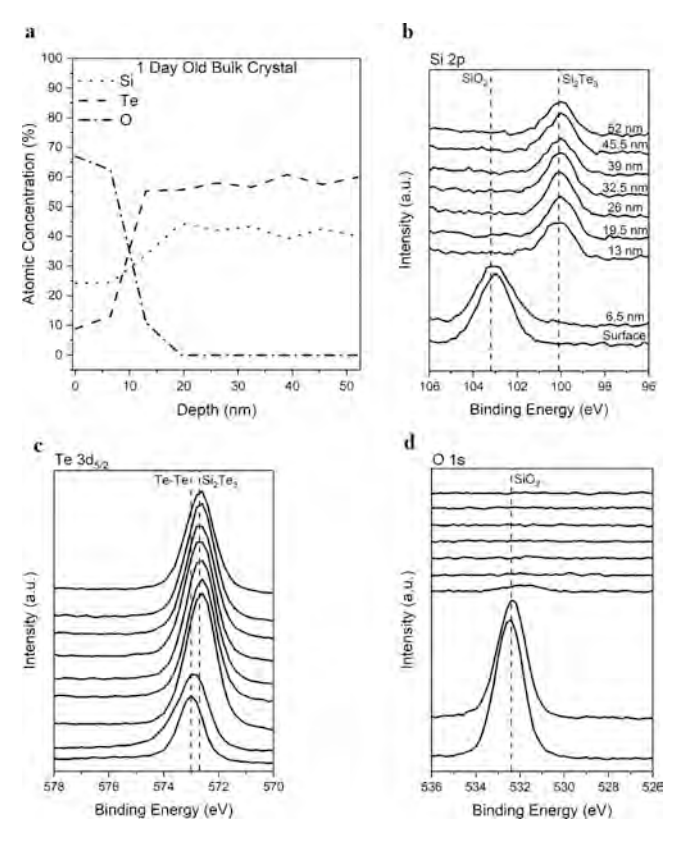


Figure 7. XPS (a) depth profile and analysis of (b) Si, (c) Te, and (d) O for one-day-old Si_2Te_3 bulk crystals on a Si substrate.

material to completely remove the oxygen-rich degraded layers and return to the pristine 2:3, silicon to tellurium, stoichiometry. This reduction in the thickness of the degraded layers of bulk $\mathrm{Si_2Te_3}$ as compared to the thin film shows that the bulk crystal degrades at a slower rate than that of the thin film.

The surface peak positions shown in the XPS analysis in Figure 7b–d are consistent with those found in the thin film with SiO_2 -associated peaks located at approximately 103.2 and 532.4 eV for the Si 2p and O 1s peaks, respectively, and at 573.0 eV for the Te–Te-associated Te $3d_{5/2}$ peak. At a depth of 19.5 nm, the SiO_2 -related peaks completely disappear, and the Si_2Te_3 -associated peaks emerge at 572.7 eV for the Te $3d_{5/2}$ peak and at 100.1 eV for the Si 2p peak.

In order to further elucidate the cause of the change in composition and Raman spectra of Si₂Te₃ with age, exfoliated flakes of Si₂Te₃ were annealed at 200 °C for 5 min under varying atmospheric conditions. Raman spectra were taken before and after annealing, and the results can be seen in Figure 8. The figure shows the emergent Raman peaks associated with tellurium only after being annealed under ambient air and water vapor-rich environments. Annealing in O₂, N₂, and vacuum resulted in no significant change in the Raman spectra. From these data, it is clear that the change seen in the Raman spectra and composition of Si₂Te₃ as samples age is primarily due to the reaction with water vapor rather than any other existing oxidizing agent.

UV-vis-NIR spectroscopy was performed on thin films of Si₂Te₃ to see how the absorbance and, by extension, the band gap evolve as the thin film degrades. Figure S7 in the Supporting Information shows pictures of the freshly grown and aged samples. Figure 9a,b shows the absorbance and the

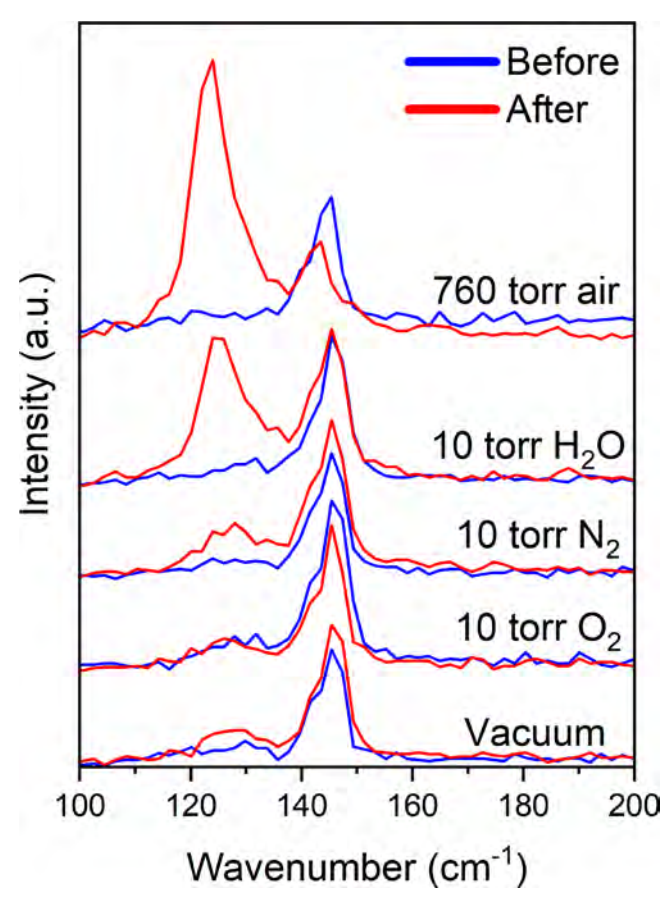


Figure 8. Raman spectra taken of exfoliated Si₂Te₃ flakes before and after annealing under different atmospheric conditions.

corresponding Tauc plots for a Si₂Te₃ thin film deposited on a glass substrate immediately after growth and after being aged for up to 8 days. After one day, the absorbance can be seen increasing, while after 4 days, it decreases. This behavior can be explained by the convolution of two separate absorption bands belonging to pristine Si₂Te₃ and tellurium. After one day, a thin degraded layer containing tellurium forms at the surface of the film resulting in an increase in the absorption band of tellurium, while the Si₂Te₃ absorption band remains relatively unchanged because the lower layers of the film remain pristine. The convolution of these two absorption bands leads to an overall increase in the absorption of the thin film. After 4 days, the absorption band due to Si₂Te₃ disappears because the film has now completely degraded. This leads to an overall decrease in the absorption, particularly in the region below 550 nm where the Si₂Te₃ band was previously located.

The Tauc plot for the fresh sample (Figure 9b) shows an estimated direct band gap of 2.15 eV, which is close to the expected value of 2.0 eV for pristine Si₂Te₃.³⁷ After 8 days, the shape of the absorption edge is consistent with that of an indirect band gap, and the calculated band gap decreases to a value of 0.517 eV (Figure 9b). This is, again, consistent with the formation of crystalline tellurium, which has a slightly indirect band gap with a value of approximately 0.35 eV.³⁸ This change in absorbance and band gap coincides with the change in color of the sample as demonstrated in Figure S7 in the Supporting Information, indicating that the change in color is due to the formation of tellurium as a result of the hydrolysis of Si₂Te₃.¹⁵ Because the photoluminescence of Si₂Te₃ is dominated by defect emission, rather than the band gap

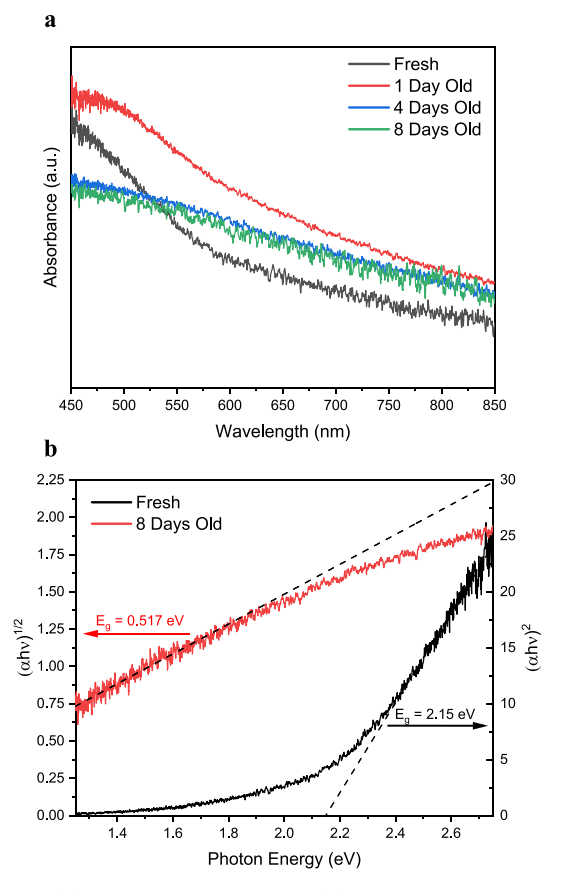


Figure 9. (a) Absorbance spectra and (b) Tauc plots for Si₂Te₃ thin films of varying age deposited on a glass substrate.

emission, this change in the band gap as samples age has previously gone undetected.

UV—vis—NIR spectroscopy was also performed on a $\rm Si_2Te_3$ flake of varying age, which was exfoliated from a bulk crystal using a typical scotch tape method. Figure S8 in the Supporting Information shows pictures of the freshly exfoliated and aged sample. Figure 10 shows the absorbance spectra taken of the exfoliated flake directly after transfer and after being aged for up to 29 days. The absorbance shows two

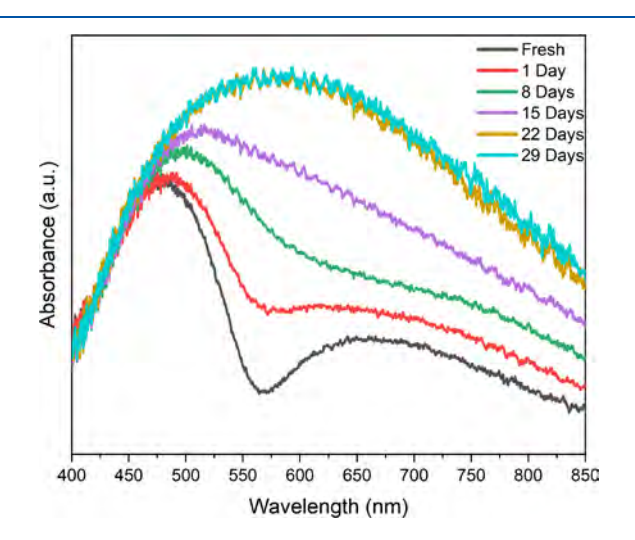


Figure 10. Absorbance spectra of Si₂Te₃ exfoliated flakes transferred to a glass substrate.

absorption bands with centers located at approximately 475 and 675 nm corresponding to $\mathrm{Si_2Te_3}$ and Te precipitates, respectively. Due the significant sub-band gap absorption of the Te precipitates, a modified Tauc procedure described by Makuła et al. was used in order to better estimate the direct band gap. In this method, the sub-band gap absorption is used as a baseline, and the intersection of this baseline with the linear fit of the direct band gap absorption edge gives an estimate of the direct band gap.

This method is demonstrated in Figure 11a, and the corresponding calculated band gap energies are displayed in

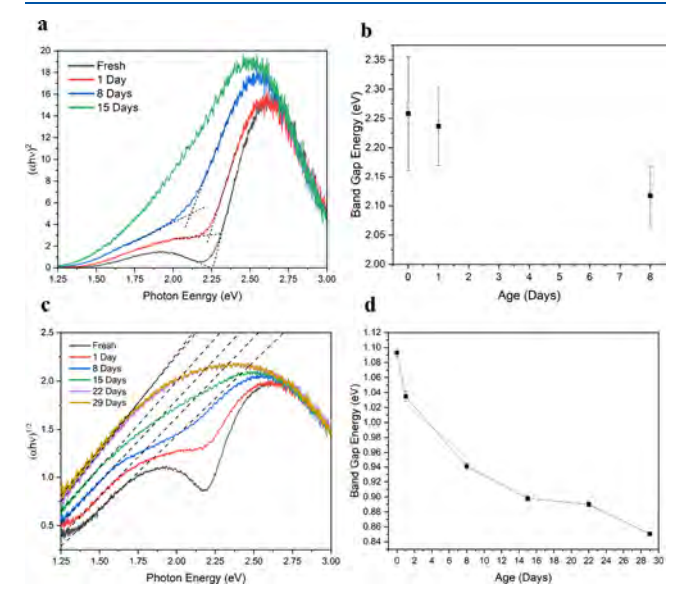


Figure 11. (a) Direct transition Tauc plot for freshly exfoliated flakes. (b) Calculated direct band gap energy vs age plot. (c) Indirect transition Tauc plot for exfoliated flakes aged up to 29 days. (d) Calculated indirect band gap energy vs age plot.

Figure 11b. The error bars in Figure 11b were found by first detemining the uncertanty in the α (photon energy) and γ ($(\alpha h \nu)^2$) coordinates due to the resolution of the spectrometer (2 nm) using the propagation of uncertainty. Then, the baseline and direct band edge were fit using the computational method of Fasano and Vio⁴⁰ for fitting a line with errors on both coordinates implemented in OriginLab Pro. Finally, the error in the intercept between the baseline and direct absorption edge fit was calculated using the propagation of the standard errors of the linear regressions. This method accounts for both the uncertainty due to the resolution of the spectrometer and for the standard error in the linear regression.

This fitting method cannot be applied after 15 days because, as seen in Figure 11a, the sub-band gap emmsion completely obscures the direct band gap absorption edge, making an accurate fitting impossible. The calculated direct band gap values are fairly constant (\sim 2.2 eV) within the determined error. This is expected because the degraded surface layers of Si₂Te₃ should not significantly affect the intrinsic band gap of the underlying pristine material. After 29 days, the absorption band belonging to Si₂Te₃ remains, although it is convoluted with and obscured by the increasing absorption from tellurium, showing that pristine Si₂Te₃ remains beneath the degraded layers of the flake. This is quite different from the behavior of this same band seen in the thin film sample (Figure 9a), which

dissapears after only 4 days. This again demonstates the thin film's elevated sensitivity when compared to the exfoliated flakes.

Figure 11c,d shows the Tauc plots and corresponding calculated indirect band gaps for the tellurium-associated absorption band. The error bars in Figure 11d were calculated in a similar fashion to those of Figure 11b, except that the propagation of error was determined for the α -intercept of the linear fit of the indirect absorption edge rather than for the intercept between the sub-band gap baseline and direct absorption edge fit. The resulting calculated indirect band gap decreases asymtotically from 1.064 to 0.828 eV after 29 days. The decrease in the rate of degradation suggests that the outer degraded layers offer some form of protection against further degradation by isolating underlying pristine Si₂Te₃ from moisture in air.

A similar decrease in the band gap has also been observed in GaTe after degradation and was determined to be a result of the chemiabsorbtion of oxygen forming GaTe-O₂. However, since our XPS and Raman data clearly show that the degraded layers of Si₂Te₃ consist primarily of Te, TeO₂, and SiO₂, this explanation is unlikely. Instead, because the intensity of this peak increases with age and because both SiO₂⁴¹ and TeO₂⁴² have band gaps much larger than 0.828 eV, we can safely conclude that this emerging absorption edge is due to elemental tellurium within the degraded layers of Si₂Te₃. This is further evidenced by the fact that monolayer tellurium has been shown to have a band gap of ~1.2 eV, which gradually decreases with each additional layer until reaching the bulk band gap of 0.35 eV. 43 Because of this, the gradual decrease in the band gap energy can best be explained by the gradual increase in the amount of elemental tellurium.

To see how the crystal structure evolves as Si₂Te₃ degrades, XRD spectra were taken for freshly grown and aged thin film samples deposited on glass substates (Figure 11). When compared to reference spectra (PDF no. 00-022-1323) for Si₂Te₃, the experimental XRD peaks located at 13.5, 24.2, 26.8, 27.8, 36.3, 40.5, 42.5, 47.6, 50.8, 51.4, 54.7, 60.6, 65.5, 68.5, 69.9, 71.4, 75.1, 81.0, and 86.8° can be assigned as the (002), (110), (004), (112), (114), (006), (300), (116), (304), (222), (008), (118), (226), (412), (0,0,10), (308), (1,1,10), (416), and (0,0,12) planes of Si₂Te₃, respectively. Only the most intense peaks are labeled in Figure 12. The thin film shows a clear growth preference along the (001) direction, while the existence of other planes confirms the film's polycrystalline nature. Rietveld refinement was performed with MDI Jade 8.8 software using PDF no. 00-022-1323 as the reference for refinement.44 The lattice was found to be hexagonal with lattice constants $a = 7.409 \pm 0.013$ Å and $c = 13.464 \pm 0.024$ Å, which is in close agreement with previously published results for silicon telluride.44

As the sample ages, the peak intensity for all peaks decreases, and no new peaks emerge. This same behavior was again seen in GaTe and was attributed to the chemiabsorption of oxygen forming GaTe-O₂. However, as previously shown, this explanation is unlikely. Instead, this decrease in intensity is likely caused by the disordering of the surface layers of Si₂Te₃ and an overall decrease in the amount of Si₂Te₃. New peaks for SiO₂ are not seen after degradation because the SiO₂ formed from hydrolysis would be amorphous as confirmed by the absence of SiO₂ in the degraded Raman spectra. No new emergent peaks for tellurium are seen most likely because the amount of tellurium, which remains in the sample, is small and

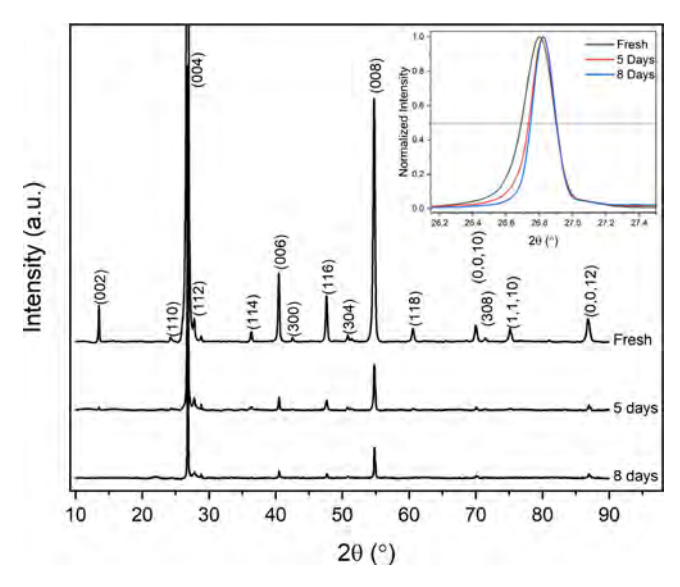


Figure 12. XRD of a Si₂Te₃ thin film deposited on glass at varying stages of degradation.

because the crystallites of tellurium formed in the degraded layers are of very small size leading to the peaks being both very weak and broad and therefore difficult to resolve.

The FWHM of each (004) peak was found by fitting with a pseudo-Voigt function using MDI Jade 8.8 software with skewness uncontrained in order to account for the asymmetry in each peak. From the inset in Figure 11, it is clear that as the sample ages, the peak shape becomes more symmetric, and the FWHM decreases. From the FWHM's, the average crystallite grain size was estimated using the Scherrer equation and was determined to be 90.2, 110.3, and 124.1 nm for the fresh, 4 day-, and 8-day-old samples, respectively. It is known that the average grain size of thin films will increase asymtotically with time until the average grain size is approximatly the same as the film thickness.⁴⁵ This increase in grain size is caused by a relaxation at grain boundaries, which results in an overall decrease in the average grain boundary energy. 45,46 Interestingly, the change in peak shape from asymmetric to symmetric could also be consistent with a relaxtion of nonuniform lattice strain and a decrease in the number of planar faults.⁴⁷ From these data, we conclude that at the same time that the surface layers are degrading, resulting in a decrease in the amount of Si₂Te₃, the pristine inner domains are coalecsing, resulting in an overall increase in the average grain size of the remaining Si₂Te₃.

4. CONCLUSIONS

This study for the first time describes a modified CVD growth method for the production of high-quality bulk and thin film $\mathrm{Si_2Te_3}$. We also offer, for the first time, a comprehensive and multimodal explanation of the mechanisms involved in the degradation of $\mathrm{Si_2Te_3}$ and, by extension, offer similar insights into other tellurium-containing materials. All results are consistent with hydrolysis resulting in the formation of a very thin surface layer of $\mathrm{TeO_2}$ and $\mathrm{SiO_2}$ followed by a thicker degraded layer, which extends into the bulk of the material consisting of Te and $\mathrm{SiO_2}$. It is shown that the bulk degraded layers are deficient in Te due to the sublimation of $\mathrm{H_2Te}$ from the surface. The remaining Te, which does not escape from the surface, is shown to be responsible for the controversial Raman

peaks at ~120 and ~140 cm⁻¹, which appear in myriad tellurium-containing compounds. Annealing in various atmospheric conditions confirmed that water vapor is the main oxidizing agent responsible for the changes in the Raman spectra and composition of aged samples. The physical understanding achieved in this work can be applied to other tellurium-containing materials.

ASSOCIATED CONTENT

Solution Supporting Information

The Supporting Information is available free of charge at https://pubs.acs.org/doi/10.1021/acs.jpcc.3c01864.

AFM cross-sectional profiles for etch depth calibration; bulk crystal and thin film optical images; thin film SEM images; thin film AFM and Te XPS depth profile including the $3d_{3/2}$ peak; Raman spectra; thin film and exfoliated flake optical images before and after degradation (PDF)

AUTHOR INFORMATION

Corresponding Author

Jingbiao Cui — Department of Physics, University of North Texas, Denton, Texas 76203, United States; orcid.org/0000-0003-3408-1016; Email: jingbiao.cui@unt.edu

Authors

Evan Hathaway – Department of Physics, University of North Texas, Denton, Texas 76203, United States; orcid.org/ 0009-0008-0048-9690

Roberto Gonzalez Rodriguez — Department of Physics, University of North Texas, Denton, Texas 76203, United States; orcid.org/0000-0001-6849-1799

Yuankun Lin — Department of Physics, University of North Texas, Denton, Texas 76203, United States; ⊚ orcid.org/ 0000-0001-5691-589X

Complete contact information is available at: https://pubs.acs.org/10.1021/acs.jpcc.3c01864

Notes

The authors declare no competing financial interest.

ACKNOWLEDGMENTS

This work was supported by the U.S. National Science Foundation with award no. 2128367.

REFERENCES

- (1) Manjón, F. J.; Gallego-Parra, S.; Rodríguez-Hernández, P.; Muñoz, A.; Drasar, C.; Muñoz-Sanjosè, V.; Oeckler, O. Anomalous Raman modes in tellurides. *J. Mater. Chem. C* **2021**, *9*, 6277–6289.
- (2) Hathaway, E.; Chen, J.; Gonzalez-Rodriguez, R.; Lin, Y.; Cui, J. Raman study of silicon telluride nanoplates and their degradation. *Nanotechnology* **2022**, *33*, 265703.
- (3) Larramendi, E. M.; Berth, G.; Wiedemeier, V.; Hüsch, K. P.; Zrenner, A.; Woggon, U.; Tschumak, E.; Lischka, K.; Schikora, D. Intensity enhancement of Te Raman modes by laser damage in ZnTe epilayers. *Semicond. Sci. Technol.* **2010**, *25*, No. 075003.
- (4) Artamonov, V. V.; Valakh, M. Y.; Strel'chuk, V. V.; Baidullaeva, A.; Mozol, P. E. Raman scattering by tellurium films on CdTe single crystals. *J. Appl. Spectrosc.* **1988**, *48*, 653–655.
- (5) Zitter, R. N. Raman detection of tellurium layers on surfaces of CdTe. Surf. Sci. 1971, 28, 335–338.
- (6) Yang, S.; Cai, H.; Chen, B.; Ko, C.; Özçelik, V. O.; Ogletree, D. F.; White, C. E.; Shen, Y.; Tongay, S. Environmental stability of 2D

- anisotropic tellurium containing nanomaterials: anisotropic to isotropic transition. *Nanoscale* **2017**, *9*, 12288–12294.
- (7) Fonseca, J. J.; Tongay, S.; Topsakal, M.; Chew, A. R.; Lin, A. J.; Ko, C.; Luce, A. V.; Salleo, A.; Wu, J.; Dubon, O. D. Bandgap Restructuring of the Layered Semiconductor Gallium Telluride in Air. *Adv. Mater.* **2016**, *28*, 6465–6470.
- (8) Berchenko, N.; Vitchev, R.; Trzyna, M.; Wojnarowska-Nowak, R.; Szczerbakow, A.; Badyla, A.; Cebulski, J.; Story, T. Surface oxidation of SnTe topological crystalline insulator. *Appl. Surf. Sci.* **2018**, 452.
- (9) Khoo, C. Y.; Liu, H.; Sasangka, W.; Made, I. R.; Tamura, N.; Kunz, M.; Budiman, A.; Gan, C. L.; Thompson, C. Impact of deposition conditions on the crystallization kinetics of amorphous GeTe films. *J. Mater. Sci.* **2016**, 51.
- (10) Goncalves, L. M.; Alpuim, P.; Rolo, A. G.; Correia, J. H. Thermal co-evaporation of Sb2Te3 thin-films optimized for thermoelectric applications. *Thin Solid Films* **2011**, *519*, 4152–4157.
- (11) Cape, J. A.; Hale, L. G.; Tennant, W. E. Raman scattering studies of monolayer-thickness oxide and tellurium films on PbSnTe. *Surf. Sci.* 1977, 62, 639–646.
- (12) Sans, J. A.; Vilaplana, R.; da Silva, E. L.; Popescu, C.; Cuenca-Gotor, V. P.; Andrada-Chacón, A.; Sánchez-Benitez, J.; Gomis, O.; Pereira, A. L. J.; Rodríguez-Hernández, P.; et al. Characterization and Decomposition of the Natural van der Waals SnSb2Te4 under Compression. *Inorg. Chem.* **2020**, *59*, 9900–9918.
- (13) Dzhagan, V.; Kapush, O.; Mazur, N.; Havryliuk, Y.; Danylenko, M. I.; Budzulyak, S.; Yukhymchuk, V.; Valakh, M.; Litvinchuk, A. P.; Zahn, D. R. T. Colloidal Cu-Zn-Sn-Te Nanocrystals: Aqueous Synthesis and Raman Spectroscopy Study. *Nanomaterials* **2021**, *11*, 2923
- (14) Pareek, D.; Balasubramaniam, K. R.; Sharma, P. Synthesis and characterization of kesterite Cu2ZnSnTe4 via ball-milling of elemental powder precursors. *RSC Adv.* **2016**, *6*, 68754–68759.
- (15) Bailey, L. G. Preparation and properties of silicon telluride. *J. Phys. Chem. Solids* **1966**, *27*, 1593–1598.
- (16) Shen, X.; Puzyrev, Y. S.; Combs, C.; Pantelides, S. T. Variability of structural and electronic properties of bulk and monolayer Si2Te3. *Appl. Phys. Lett.* **2016**, *109*, 113104.
- (17) Wang, M.; Lahti, G.; Williams, D.; Koski, K. J. Chemically Tunable Full Spectrum Optical Properties of 2D Silicon Telluride Nanoplates. *ACS Nano* **2018**, *12*, 6163–6169.
- (18) Chen, J.; Bhattarai, R.; Cui, J.; Shen, X.; Hoang, T. Anisotropic optical properties of single Si2Te3 nanoplates. *Sci. Rep.* **2020**, *10*, 19205
- (19) Tamalampudi, S. R.; Dushaq, G.; Villegas, J. E.; Paredes, B.; Rasras, M. S. Si2Te3 Photodetectors for Optoelectronic Integration at Telecommunication Wavelengths. *IEEE J. Sel. Top. Quantum Electron.* **2022**, 28, 1–7.
- (20) Chen, J.; Tan, C.; Li, G.; Chen, L.; Zhang, H.; Yin, S.; Li, M.; Li, L.; Li, G. 2D Silicon-Based Semiconductor Si2Te3 toward Broadband Photodetection. *Small* **2021**, *17*, No. 2006496.
- (21) wu, K.; Jiyang, C.; Shen, X.; Cui, J. Resistive switching in Si 2 Te 3 nanowires. AIP Adv. 2018, 8, 125008.
- (22) Frisenda, R.; Niu, Y.; Gant, P.; Molina-Mendoza, A. J.; Schmidt, R.; Bratschitsch, R.; Liu, J.; Fu, L.; Dumcenco, D.; Kis, A.; et al. Micro-reflectance and transmittance spectroscopy: a versatile and powerful tool to characterize 2D materials. *J. Phys. D: Appl. Phys.* 2017, 50, No. 074002.
- (23) Song, X.; Ke, Y.; Chen, X.; Liu, J.; Hao, Q.; Wei, D.; Zhang, W. Synthesis of Large-Area Uniform Si2Te3 Thin Film for p-type Electronic Device. *Nanoscale* **2020**, 12.
- (24) Lin, C.-Y.; Ulaganathan, R. K.; Sankar, R.; Murugesan, R. C.; Subramanian, A.; Rozhin, A.; Firdoz, S. Silicon-based two-dimensional chalcogenide of p-type semiconducting silicon telluride nanosheets for ultrahigh sensitive photodetector applications. *J. Mater. Chem. C* **2021**, *9*, 10478–10486.
- (25) Wu, K.; Sun, W.; Jiang, Y.; Chen, J.; Li, L.; Cao, C.; Shi, S.; Shen, X.; Cui, J. Structure and photoluminescence study of silicon

based two-dimensional Si2Te3 nanostructures. J. Appl. Phys. 2017, 122, No. 075701.

- (26) Zwick, U.; Rieder, K. H. Infrared and Raman study of Si2Te3. Zeitschrift für Physik B Condensed Matter 1976, 25, 319-322.
- (27) Martin, R. M.; Lucovsky, G.; Helliwell, K. Intermolecular bonding and lattice dynamics of Se and Te. *Phys. Rev. B* **1976**, *13*, 1383–1395.
- (28) Du, Y.; Qiu, G.; Wang, Y.; Si, M.; Xu, X.; Wu, W.; Ye, P. D. One-Dimensional van der Waals Material Tellurium: Raman Spectroscopy under Strain and Magneto-Transport. *Nano Lett.* **2017**, *17*, 3965–3973.
- (29) Richter, W. Extraordinary phonon Raman scattering and resonance enhancement in tellurium. *J. Phys. Chem. Solids* **1972**, 33, 2123–2128.
- (30) Ciesielski, A.; Skowronski, L.; Pacuski, W.; Szoplik, T. Permittivity of Ge, Te and Se thin films in the 200–1500 nm spectral range. Predicting the segregation effects in silver. *Mater. Sci. Semicond. Process.* **2018**, *81*, 64–67.
- (31) Li, J.; Lian, K. The effect of SiO2 additives on solid hydroxide ion-conducting polymer electrolytes: a Raman microscopy study. *Phys. Chem. Chem. Phys.* **2018**, *20*, 7148–7155.
- (32) Sirotti, F.; De Santis, M.; Rossi, G. Synchrotron-radiation photoemission and x-ray absorption of Fe silicides. *Phys. Rev. B* **1993**, 48, 8299–8306.
- (33) Powell, C. J. Recommended Auger parameters for 42 elemental solids. *J. Electron Spectrosc. Relat. Phenom.* **2012**, *185*, 1–3.
- (34) Chowdari, B. V. R.; Pramoda Kumari, P. Thermal, electrical and XPS studies of Ag2O·TeO2·P2O5 glasses. *J. Non-Cryst. Solids* **1996**, 197, 31–40.
- (35) Lisovskyy, I.; Voitovych, M.; Sarikov, A.; Litovchenko, V. G.; Romanyuk, A.; Melnyk, V.; Khatsevich, I.; Shepeliavyi, P.; Lashkarev, V. Transformation of the structure of silicon oxide during the formation of Si nanoinclusions under thermal annealings. *Ukr. J. Phys.* **2009**, *54*, 383–390.
- (36) Novikov, Y. N.; Gritsenko, V. A. Short-range order in amorphous SiOx by x ray photoelectron spectroscopy. *J. Appl. Phys.* **2011**, *110*, No. 014107.
- (37) Lambros, A. P.; Economou, N. A. The Optical Properties of Silicon Ditelluride. *Phys. Status Solidi B* **1973**, *57*, 793–799.
- (38) Coker, A.; Lee, T.; Das, T. P. Investigation of the electronic properties of tellurium—energy-band structure. *Phys. Rev. B* **1980**, *22*, 2968–2975.
- (39) Makuła, P.; Pacia, M.; Macyk, W. How To Correctly Determine the Band Gap Energy of Modified Semiconductor Photocatalysts Based on UV–Vis Spectra. J. Phys. Chem. Lett. **2018**, *9*, 6814–6817.
- (40) Fasano, G.; Vio, R. Fitting a Straight Line with Errors on both Coordinates. Bulletin d'Information du Centre de Donnees Stellaires 1988, 35, 191.
- (41) Weinberg, Z. A.; Rubloff, G. W.; Bassous, E. Transmission, photoconductivity, and the experimental band gap of thermally grown SiO₂ films. *Phys. Rev. B* **1979**, *19*, 3107–3117.
- (42) Moufok, S.; Kadi, L.; Amrani, B.; Khodja, K. D. Electronic structure and optical properties of TeO2 polymorphs. *Results Phys.* **2019**, *13*, No. 102315.
- (43) Wang, Y.; Qiu, G.; Wang, R.; Huang, S.; Wang, Q.; Liu, Y.; Du, Y.; Goddard, W. A.; Kim, M. J.; Xu, X.; et al. Field-effect transistors made from solution-grown two-dimensional tellurene. *Nat. Electron.* **2018**, *1*, 228–236.
- (44) Haneveld, A. J. K.; van der Veer, W.; Jellinek, F. On silicon tritelluride, Si2Te3, and alleged phosphorus tritelluride. *Recl. Trav. Chim. Pays-Bas* **1968**, 87, 255–256.
- (45) Thompson, C. V. Grain Growth in Thin Films. *Annu. Rev. Mater. Sci.* **1990**, 20, 245–268.
- (46) Chaudhari, P. Grain Growth and Stress Relief in Thin Films. J. Vac. Sci. Technol. 1972, 9, 520–522.
- (47) Simm, T. H. Peak Broadening Anisotropy and the Contrast Factor in Metal Alloys. *Crystals* **2018**, *8*, 212.

□ Recommended by ACS

Mesoporous Semiconductive Bi₂Se₃ Films

Tomota Nagaura, Yusuke Yamauchi, et al.

JUNE 08, 2023

NANO LETTERS

READ 🗹

Fabrication of Spindt-Type Nanometer-Sized Chromium Tips for Application as Field-Electron Emitters by Releasing the Stress of the Deposited Thin Film

Jinlun Huang, Shaozhi Deng, et al.

DECEMBER 21, 2022

ACS APPLIED NANO MATERIALS

READ 🗹

Self-Organized Nanocomposite Structure Controlled by Elemental Site Occupancy to Improve Vortex Pinning in YBa₂Cu₃O₇ Superconducting Films

Tomoya Horide, Kaname Matsumoto, et al

MAY 25, 2022

ACS APPLIED ELECTRONIC MATERIALS

READ [7

Nanoscale Characterization of Chemical and Structural Properties of the $Au/(100)\ \beta\text{-}Ga_2O_3$ Interface

Luke A. M. Lyle, Lisa M. Porter, et al.

AUGUST 30, 2022

ACS APPLIED ELECTRONIC MATERIALS

READ 🗹

Get More Suggestions >